

MAIN ROTOR AND TAIL ROTOR BLADE VORTEX INTERACTION NOISE UNDER THE INFLUENCE OF THE FUSELAGE

Jianping Yin

DLR, Institute of Aerodynamics and Flow Technology, Helicopter Division,

Lilienthalplatz 7, 38108 Braunschweig, Germany

Jianping.Yin@dlr.de

ABSTRACT

This paper addresses the effects of the fuselage on the mutual interference between main rotor (MR) and tail rotor (TR), their shed wakes as well as noise characteristics. For this purpose, a BO105 MR/TR/Fuselage configuration is chosen in the numerical simulations. An unsteady free wake 3-D panel method (UPM) is used to account non-linear effects associated with the mutual interference between MR/TR/Fuselage as well as development of MR/TR shed wakes. Free wake and rotor noise computations were performed to study the effect of MR/TR/Fuselage mutual interaction on rotor wake development, blade loads and noise radiation. The sound propagation into the far field is calculated with DLR FW-H code APSIM by using UPM unsteady blade pressure as input. The effect of the fuselage, tail boom and stabilizers on MR/TR aerodynamic (unsteady blade loads, wake development) will be discussed and compared with HELINOVI wind tunnel measured data. In addition, tip vortex core radius development model derived from experiment has been calibrated. The numerical results indicate that in 6° descent flight where MR is major source of noise, inclusion of the fuselage in the simulation has in general improved clearly the correlation against the measured data and caused a reduction of MR BVI at advancing side and therefore improves comparison of maximum BVI noise level with experiment, while in low speed climb and high speed level flight where TR is major source of noise, the effect of the fuselage increases slightly TR BVI at advancing side when TR blade passes over the vertical stabilizer and therefore causes increasing TR BVI noise. The study on change TR rotational direction indicated aerodynamic interaction between the main and tail rotors is sensitive to the tail rotor rotational direction. The reduction of TR BVI amplitude and number of TR BVIs on the advancing TR blade side in TR rotating in Advancing Side Up (ASU) is the cause of a significant aerodynamically-induced loading noise reduction. The comparison between the experimental results and the numerical ones highlighted once more the extreme complexity of the aerodynamic phenomena involved in a complete helicopter configuration operating at different flight conditions.

ABBREVIATIONS

MR	Main Rotor
TR	Tail Rotor
UPM	Unsteady Panel Method
ASD	Advancing Side Down (= bottom blade forward)
ASU	Advancing Side Up (= top blade forward)
BVI	Blade Vortex Interaction
ADV	Advancing side
RET	Retreating side
FUS	Fuselage
rev	revolution
RPM	Rotor rotations per minute
r_c	Tip vortex core size
r_{c0}	Initial tip vortex core size
ψ	Azimuth angle
θ	Blade collective pitch
β	Blade flap angle

1. INTRODUCTION

Aerodynamic interference plays an important role in full helicopter configurations. The closely arranged main rotor (MR) and tail rotor (TR), the submergence of the tail rotor in

the main rotor wake, and finally the interference with the fuselage, tail boom and empennage (rear lift surfaces and stabilizers) constitutes the mixture of complicated aerodynamic interactions involved in all flight conditions of helicopters.

The aerodynamic interference, like MR/TR, the MR/Fuselage interaction and the TR/Fin blockage, can affect the design of the helicopter as well as the overall helicopter noise; but the main research efforts in the past were concentrated either on the MR/Fuselage interaction noise, where extensive work, both theoretical and experimental helped to deepen the understanding of its nature effect on the aerodynamic performance and the noise generating mechanisms [1,2,3,4], or on MR/TR interaction noise [5,6,7,8] without taking into account on the influence of fuselage and fin on TR noise. Although the experiment studied shows that the installation of the tail rotor empennage (pylon and stabilizer) increased TR noise level [1], the research effort towards MR/TR interaction noise under influence of fuselage and fin has been less. The reason is that the complex flow surrounding the TR poses an extreme challenge for both experimental and theoretical studies as the flow around TR is the sum of the interacting

flows generated by the MR wake, fuselage, rotor hub, engine exhaust and empennage flows in addition to its own wake.

The studies on the effect of MR/Fuselage and MR Hub on MR Blade-Vortex Interaction airloads made by Lim, Boyd and Jung et al. [2,3,4] indicated that the rotor-fuselage model improves the correlation significantly in terms of magnitudes and phases of the airloads solution compared to the isolated rotor model. The blade-vortex interaction (BVI) peaks and phase are better captured, while the presence of a rotor hub had a negligible effect on rotor airloads and trim values [2]. In addition, the fuselage showed only marginal influence on blade motions and structural moments. However, the effects of fuselage on MR noise radiation evaluation have not yet been conducted in these studies.

Theoretical analysis of MR/TR interaction noise considered in most of previous investigations is based on the models of MR/TR and focus on the interactional effects on the aerodynamics and noise characteristics [9,10,11,12,13,14, 15]. Studies recognized that the tail rotor is an important noise source and its aeroacoustic simulation is very challenging but at the same time does not allow figuring out a general rule about the TR interactional aeroacoustic effects. The TR acoustics, indeed, is also strongly dependent on the helicopter configuration and trim parameters.

The present work is an extension of the authors' previous works [5,7]. A BO105 MR/TR/Fuselage configuration is chosen in the numerical simulations as shown in Figure 1. MR/TR aerodynamic and noise under influence of fuselage will be studied in several certification flight conditions. The comparison of rotor blade loads and flow field with EU project HELINOVI [16,17] wind tunnel measured data will be conducted. Finally tail rotor noise reduction by changing the sense of TR rotational direction will be investigated.

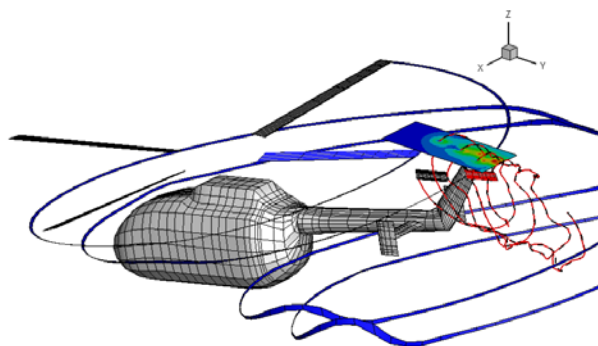


Figure 1. BO105 MR/TR/Fuselage configuration chosen in the numerical simulations

2. DESCRIPTION OF NUMERICAL SIMULATION

The numerical methodologies are to start from an unsteady free wake 3-D panel code UPM [5] which is coupled with the Ffowcs Williams-Hawkings [18] code APSIM [19,20] for predicting noise on the wind tunnel measurement plane

using unsteady blade pressure on both MR and TR as input. The rigid blade motion is applied in the simulation and the acoustic scattering of the fuselage is not accounted for. The elastic blade motion as well as acoustic scattering from fuselage will be the future topics.

2.1 Aerodynamic Model

The 3D unsteady free wake panel code, UPM [5] is used. UPM is a velocity-based, indirect potential formulation – a combination of source and dipole distribution on the solid surfaces and dipole panels in the wake.

2.1.1 Model of lifting rotor blade or wing

The model of the lifting rotor blade or wing consists of the following elements (Figure 2):

- a) A source/sink distribution over the blade surface to simulate the displacement effect of blades with finite thickness.
- b) A prescribed weighting function for the vortex strength over the blade or wing chord to account for the blade lift.
- c) A short zero-thickness elongation of the trailing edge along its bisector (Kutta panel) to satisfy the Kutta condition. The satisfaction of the flow tangency condition on the Kutta panel fixes the total strength of the circulation in the blade section; its variation over the blade chord is given by b) above. The orientation of the Kutta panel determines the direction of the emission of a wake element at the time of its release from the blade trailing edge.

The advantage of the Kutta condition application described in c) is that the additional equations expressing the Kutta condition are linear. It was found that the numerical Kutta condition without ensuring pressure equality at the trailing edge was not sufficient. An iterative scheme is implemented in order to modify the solution and ensure pressure equality at the trailing edge. This method is proved to be computationally efficient and robust with respect to the size of the time step and the number of panels on the blade.

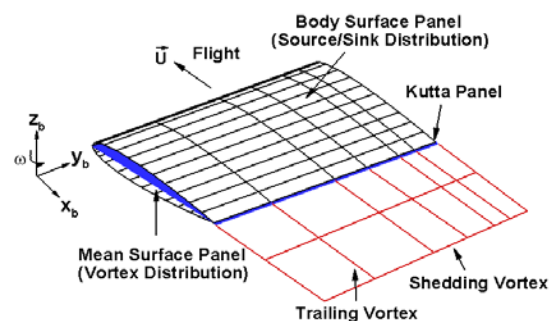


Figure 2. Numerical model of a Blade and Wake

The pressure on the blade surface is calculated using the unsteady Bernoulli equation. The non-linearity of the problem stems from the a priori unknown spatial location of the wakes. An additional complexity in the case of MR/TR operation arises due to the relative motion between the MR and TR blades, whose consideration is essential to correctly capture the interaction effects.

2.1.2 Modeling of fuselage

In the current implementation, the fuselage, tail boom and empennage are not considered as a lifting surface and thus contribute zero net vorticity to the flow. To model the presence of a fuselage, the fuselage surface is discretized into a system of N quadrilateral panels, as shown in Figure 1. Each panel is represented as a source/sink of constant strength. The velocity at any panel centroid is then given by the sum of the influences from the rotors, fuselage and wakes on the body together with the free stream component of velocity. A boundary condition of zero through flow is enforced simultaneously at the centroids of all panels.

2.1.3 Modeling of free wake generation

The free wake is represented in the form of connected vortex filaments. The model of free wake consists of following steps:

- a) At the start of the computation there are no wakes present.
- b) After the first computation step, all rotor blades or wing move to a new position with a velocity which is relative to the ground fixed frame of reference and consists of translation, rotation and other motion. Figure 2 shows the wake strip comprising a series of quadrilateral ring vortices after having been released from the downstream edge of the Kutta panel. The spanwise variation of the circulation on this new row of wake panels is the same as that on the Kutta panels and will keep unchanged throughout the whole computations.
- c) After each computation step, a new wake strip is created and added to the previous wake. The whole wake surfaces are then freely deformed according to the locally induced velocity.
- d) With the generation of the wake its induction effect is included to satisfy the flow tangency condition for the next computation step.

A full-span free wake is generated in this manner step by step behind the blades or wings as the computation proceeds. The free wake analysis requires no initial condition and is a fully interactive free wake model.

As the computation time sharply increases with increasing the length of wake, to fix the length of wakes can be used to save the computational time [15]. This is true for steady flight since general shape of developed free wake remains unchanged after several revolutions. When length of wakes,

normally number of steps used in present study, arrives at user input value (2 rotor revolutions), the oldest wake elements are discarded when new wake elements added at the end of each time step.

In MR/TR/Fuselage case, in general, the computation of MR and TR should be started simultaneously. The rotors are simply started impulsively from rest and the free wakes are generated step by step with the developing rotor motion. Usable results could only be obtained after initial wakes pass away from both rotors. In order to save CPU-time, it is helpful to start running MR/Fuselage computation independently at first several revolutions until the MR initial wakes pass through TR rotational plan and then switch on the TR computation and run MR/TR/Fuselage simultaneously.

2.1.4 Tip vortex roll-up and vortex core size

Tip vortex roll-up is modeled starting from the results of free developed wake model. Local rolling up and vorticity concentration are then modeled. One or several new vortex filaments are constructed based on the properties of the vortex lattices. These filaments simulate the actual vortices in circulation and location. Fundament of rolling up process is following the idea of Betz inviscid roll-up method for vorticity from fixed wings. Since Betz roll-up model is only suitable for the fixed wing, further conditioning of the bound circulation distribution is required to account for the fact that the blades are rotating during forward flight. The rotor wake roll-up used in present paper are described in the reference [21,22], respectively. The difference from the ref.[21, 22] is that fully free wake results have been used as the starting point to build wake roll-up [5,7].

The core radii of blade tip vortices in the rotor wake are the least known parameter to model since only very few measurements exist. The development of the tip vortex core size (or core radius) as function of time or blade azimuth angle (vortex age) was derived from HartII measurement [23] and is given by following formulation

$$(1) \quad r_c = r_{c0} * [1 + \psi / (2\pi)]$$

Where r_{c0} is initial tip vortex core size and $r_{c0} = 0.3C$ is used in present paper, where C is the chord length in the blade tip. r_{c0} is determined from a parameter study of vortex core size on BVI noise, since the induced velocity of a vortex is one of the key parameters which influence the magnitude of BVI noise. HELINOVI [16,17] 6° descent flight is used to calibrate this value. Figure 3 indicates that maximum BVI noise level is sensitive to the initial core radius and a vortex core radius of $0.3c$ generates a $BVISPL_{max}$ which is in good agreement with the experimental value. Here $BVISPL_{max}$ is maximum BVI sound pressure level chosen at advancing blade side (ADV) and covered by the frequency range from the 6th through the 40th blade passing frequency (BPF) harmonics. Following

this result, the vortex core radius of $0.3c$ was utilized in all subsequent acoustic predictions. The development of the tip vortex core radius as function of vortex age is plotted for 3 different initial core radius in Figure 4. The vertical lines indicate the area of wake ages where possible advancing side (ASD) or retreating side (RET) BVI occur. The vortex ages where retreating side and advancing side BVI occur is located from 100 to 670° of blade azimuth angle. These values were derived from the BVI position in the blade loads presented in the next sections. In general, actual vortex core size values located between 0.4 and 0.8 chord length have been used in the simulations.

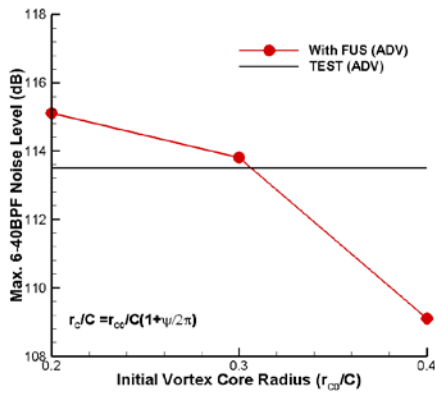


Figure 3. BVISPLmax as a function of vortex core radius for HeliNovi 6° descent flight

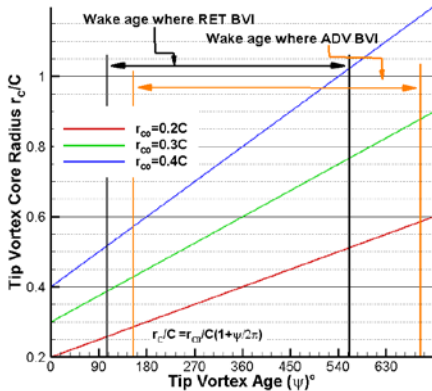


Figure 4. Development of the tip vortex core radius as function of vortex age

2.1.5 Rotor trim

In order to have a good comparison between the experimental data and the numerical simulations, the force trim according to trimmed data from the test is used. The force trimming procedure applied in numerical simulation is to adjust the pitch schedule in such a way that the thrust, pitch and roll moment of both MR and TR matches the experimental one. For a helicopter rotor the pitch schedule is

given by $\theta = \theta_0 + \theta_{1c} \cos(\psi) + \theta_{1s} \sin(\psi)$, where ψ , θ_0 , θ_{1c} , and θ_{1s} are the azimuth angle, the collective pitch, the longitudinal cyclic pitch and the lateral cyclic pitch angle respectively. Note that in the current simulation no lead-lag schedule has been used. The flap schedule has not been modified for the main rotor. For the see-saw motioned BO105 TR, the Pitch $[\theta]$ - Flap $[\beta]$ (teeter) angle coupling has been taken into account. The force trimming procedure defined a set of non-linear functions. The Newton-Raphson root-finding algorithm is used to determine the final control angle $(\theta_0, \theta_{1c}, \theta_{1s})$. In MR/TR/Fuselage interaction cases, only TR is trimmed, while the trimmed MR/Fuselage control angle is applied to MR, assuming effect of TR on MR/Fuselage trim can be neglected.

2.2 The Aeroacoustic Model

The Aeroacoustic Prediction System based on an Integral Method, APSIM [19,20], has been developed at the DLR Institute of Aerodynamics and Flow Techniques for prediction of rotor or propeller noise radiated in the free far-field. The method is designed to calculate wave propagation over large distances in uniform flows and has been extended recently to couple with CFD and CAA methods for propagating any noise signal to the far field. The methodology is based on both Ffowcs-Williams/Hawkings (FW-H) and Kirchhoff formulations and only linear sound propagation is taken into account. In general the aeroacoustic computation into the far field is split into two steps: In a first step the aerodynamic flow field or the pressure data on the body is computed by aerodynamic code and provided to APSIM; in a second step the sound propagation into the far field is calculated with APSIM.

Several additional points should be made when calculating main and tail rotor interaction noise. Firstly, when the main- and tail rotor noise are not evaluated at same time interval, the same time interval (smaller one) should be used during the computation of total time signal. Secondly, when the ratio of main and tail rotor rotational speed is not in an even number, the total acoustical signal can be added directly under frequency domain, otherwise time domain should be always used.

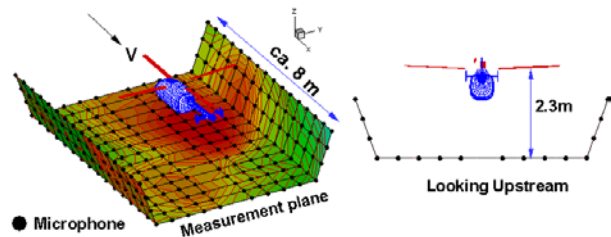


Figure 5. Wind tunnel measurement plane

2.2.1 Acoustic simulation on wind tunnel test plane

In order to make comparison with wind tunnel test results, the acoustic simulation are conducted on a near field plane

situated 1.15 MR radii below the MR hub with a range of 3.25 x 4 MR diameters as shown in Figure 5. The acoustic pressure time histories radiated from both MR and TR are first summed in time domain and transformed into a narrow band spectrum on each reference points which are located on the wind tunnel measurement plane.

2.3 Model Description

Technical data of the main rotor and tail rotor are listed in Table 1.

Property	MR	TR
no. of blades	4	2
rotor type	hingeless	teetering
radius	2 m	0,383 m
radius scale factor	2.455	2.48
chord	0.121 m	0.074 m
root cut-out	0.44 m	0.16 m
solidity	0.077	0.123
precone	2.5°	0°
pretwist	-8°/R	0°/R
pitch-flap coupling	0°	45°
tip Mach number (ISA)	0.64	0.61
lock number	8	4.2
shaft tilt forward	3°	-4°
shaft tilt upward	0°	-3°
airfoil	NACA 23012	S102E, NACA0012

Table 1 Main Rotor (MR) and Tail Rotor (TR) Data

Tail rotor was run at a slightly slower speed (approx. 6% slower) than appropriate for the scaled BO105. The objective of this is to provide an integer ratio between main and tail rotor speeds in order to facilitate numerical simulation, in this case 5 tail rotor revolutions to each main rotor revolution and results in a tail rotor tip Mach number of 0.614. It is not believed that this change has any impact on the character of the interaction between main and tail rotors.

3. RESULTS AND DISCUSSION

The effects of the fuselage on the mutual interference between MR and TR, their shed wakes as well as noise characteristics has been investigated for several HELINOVI cases, including changing TR sense of rotation.

The flight conditions chosen are a 6° descent at 33m/s (ID5) where MR BVI noise is dominant, a 12° climb at 33m/s (ID1) and a level flight at 60m/s (ID2) where the TR is major source of noise. Table 2 gives the flight conditions for baseline cases where TR blades with S102E profile are used.

ID #	Flight Cond.		Main Rotor			Tail Rotor	
	V_∞ (m/s)	θ_{FP} (deg)	$M_{\Omega R}$	$10^4 \cdot C_T$	α_{sh} (deg)	$M_{\Omega R}$	$10^4 \cdot C_T$
1	33	12	0.641	52.9	-14.6	0.614	90.9
2	60	0	0.641	52.0	-6.8	0.614	54.5
5	33	-6	0.641	50.4	3.6	0.614	27.5

Table 2 baseline flight conditions

TR blades with NACA0012 profile are employed to study the effects of different TR rotational direction.

ID #	Flight Cond.		Main Rotor			Tail Rotor	
	V_∞ (m/s)	θ_{FP} (deg)	$M_{\Omega R}$	$10^4 \cdot C_T$	α_{sh} (deg)	$M_{\Omega R}$	$10^4 \cdot C_T$
(TR ASD)	33	12	0.641	52.9	-14.7	0.614	88.8
(TR ASU)	33	12	0.641	52.9	-14.4	0.614	88.7

Table 3 flight conditions for different TR rotational direction

The computations started with a step size of 5° MR azimuth and this was reduced to 1° after initial wakes pass away from both rotors. This corresponds to a rotation of 5° of the TR. The MR blade is discretized by 26 panels along the profile contour and 9 panels along the span with totally 234 panels for each blade while each TR blade consists of 210 panels.

3.1 6° descent flight with 33m/s (ID5)

Experimental results show that MR is the dominant source of noise in this flight condition. Hence, the analysis will focus only on the effect of the fuselage on the MR for this flight condition. Figure 6 displays perspective top view of the development of MR tip vortex with the reference blade (blue) at $\psi=40^\circ$ azimuth where $\psi=0^\circ$ if the blade points downstream. The longitudinal cutting planes shown along the y-axis at $x/R=0.7$ (retreating side), and -0.7 (advancing side) demonstrate induced velocity contour plots by MR tip vortex under influence of the fuselage. There appears only small difference in the tip vortex trajectory which located in the inner part around the fuselage. Virtually there is no sensitivity to the presence of the fuselage for the outboard tip vortices which indicate azimuth position of BVI will hardly be changed.

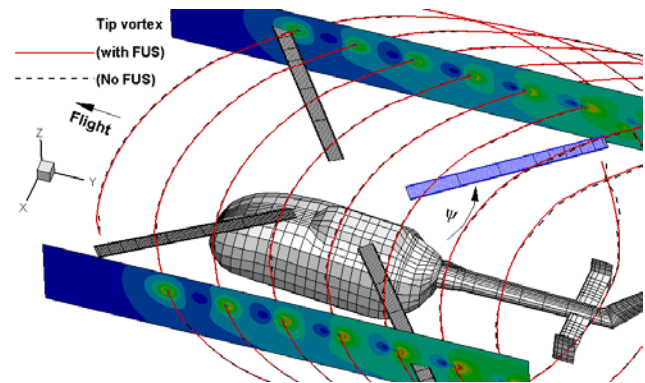


Figure 6. Perspective top view of the development of MR tip vortex with the reference blade at 40° azimuth

Figure 7 displays the enlarged closer view of the tip vortex in an advancing side BVI position at $\psi=40^\circ$ azimuth angle of the reference blade. In general the tip vortex is located above rotor tip path plane for this flight condition. Vertical displacement of the tip vortex due to the influence of the

fuselage is seen in this figure. There is a slightly larger miss distance of the tip vortex to the blade for the rotor-fuselage case. This is due to the effect of the upwash of the fuselage is to slow down the rotor downwash and the convection of the tip vortex towards the blade is reduced in rotor-fuselage case, which increases slightly the miss distance of the tip vortex to the blade. Therefore a reduction of BVI is expected in rotor-fuselage.

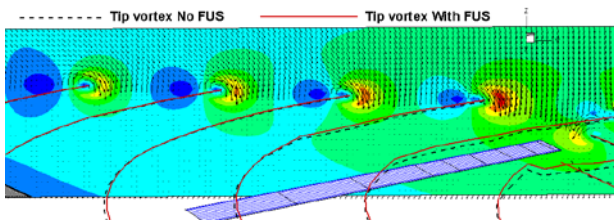


Figure 7. Enlarged closer view of the tip vortex in the advancing side BVI position at 40° azimuth

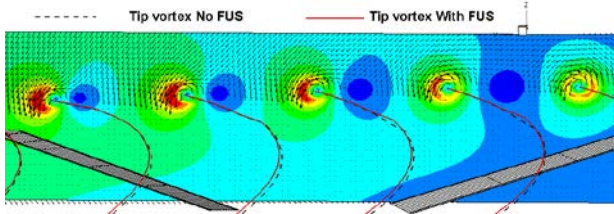


Figure 8. Enlarged closer view of the tip vortex in the retreating side

Similar tip vortex development characteristics under influence of fuselage are also observed in the retreating side as show in Figure 8.

The MR sectional normal loads C_N at 87% radial station is given in Figure 9 in one MR revolution.

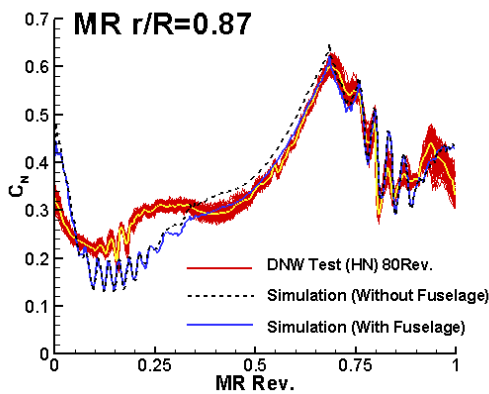


Figure 9. MR Sectional normal load

The group of red lines denotes the measured data for all 80 revolutions, while the continuous blue lines and dashed black lines denote the predicted results with the isolated rotors and rotor-fuselage models, respectively. The mean

values of the experiment averaged over 80 revolutions are shown in yellow line in Figure 9.

Figure 9 shows that inclusion of the fuselage improves clearly the correlation against the measured data in 2nd and 3rd quadrant of MR revolutions. There is over estimation on the blade normal force in these two quadrants when lack of the fuselage in the simulation. The high frequency fluctuations in both the experimental and simulated sectional load in both 1st and 4th quadrant clearly indicate the presence of strong BVI phenomena which make the MR the dominating factor of the total noise radiation during this flight condition. There is a small difference between the isolated rotor and rotor-fuselage models for the signal in both 1st and 4th quadrant

The C_{nM2} spanwise distributions at both $\psi=180$ and 220 , as shown in Figure 10 indicate that the effect of fuselage has led to high loading for the inner part of station as the fuselage upwash cancels some rotor downwash and results in high angle of attack there. With the station moved away from the fuselage towards blade tip, the effect of fuselage tends to show increase rotor downwash or decrease the angle of attack there, therefore the reduction of loading for the outer part is observed.

As the time derivative of airloads play an important role in the noise generation, the time derivative of the sectional airloads shown in Figure 9 is given in Figure 11. Figure 7 shows the enlarged views of Figure 11 focusing on either the advancing side (Figure 12left) or the retreating side (Figure 12right).

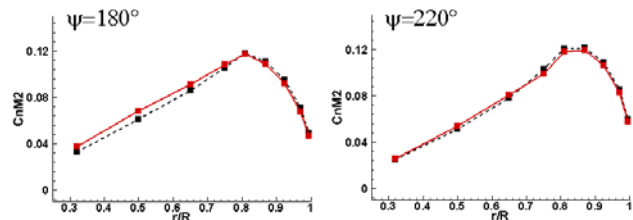


Figure 10. C_{nM2} spanwise distribution

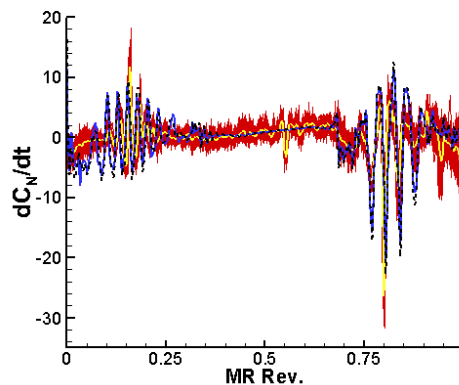


Figure 11. Time derivative of airloads

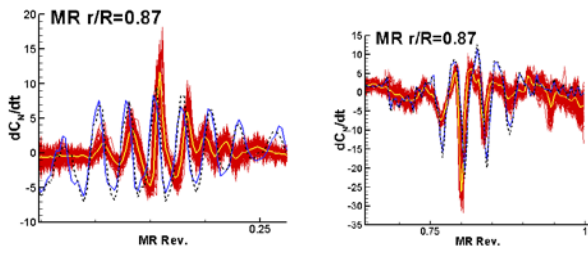


Figure 12. Enlarged views of Figure 2 for ASD side(left) and RET side (right)

The two sets of predictions track each other pretty closely with the experiment results. As appeared in the Figure 12, the number of BVI counts in both advancing and retreating side keeps the same, while peak-to-peak magnitudes of the BVI signals are slightly reduced in the rotor-fuselage model as increasing miss distance explained in Figure 7.

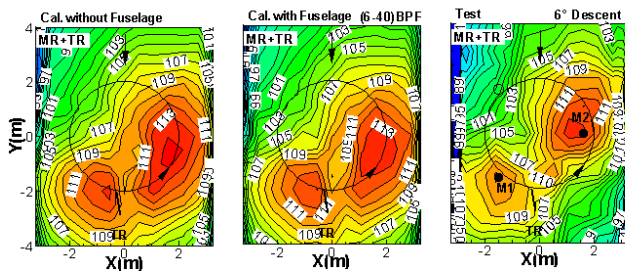


Figure 13. Simulated and measured (right) full scale dBA contours, without FUS (left) and with FUS (middle)

To gain an insight into the directivity of the generated noise under influence of the fuselage, Figure 13 compares noise contour plot for mid-frequency summary level (6thBPF-40BPF) with measurement (right). The location of the MR disc is indicated by the circle. Two maximum noise areas (hot spots) one on advancing and one on retreating side are captured in the predicted noise contour. The influence of the fuselage has in general caused a reduction of maximum MR BVI in both advancing and retreating side by 1dB, which corresponds to the reduction of BVI as observed in Figure 12.

Figure 14 gives the comparisons of the acoustic pressure time histories taken from 2 microphone positions (M1, M2), as shown in Figure 13 right. The time histories show a general agreement in both phase and amplitude with experiment.

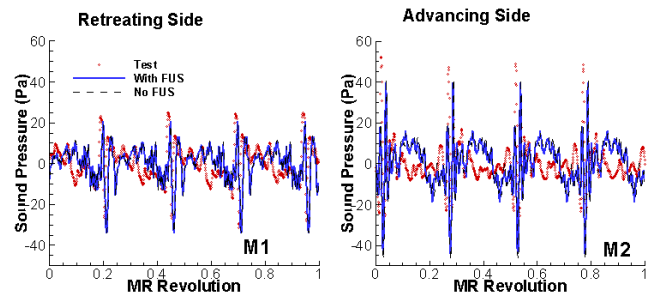


Figure 14. Acoustic pressure time histories taken from M1 and M2, as shown in Figure 13

Figure 15 shows the effect of the fuselage on maximum mid-frequency summary level at both advancing (ADV) and retreating (RET) side for different vortex core size. In general inclusion of the fuselage has improved the correlation with test results.

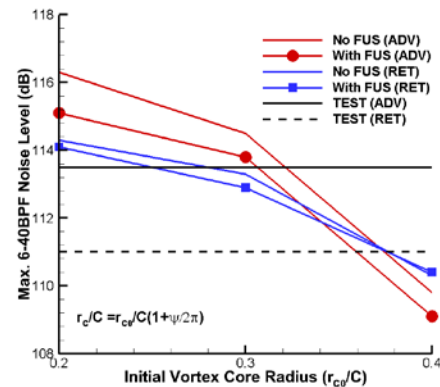


Figure 15. BVISPLmax as a function of vortex core radius for both ASD and RET side

3.2 12° climb with 33m/s (ID2)

The perspective top view of the development of MR tip vortex with the reference blade (blue) located at $\psi = 40^\circ$ azimuth angle is given in Figure 16. In this flight condition, MR tip vortex is far below the MR tip path plane in comparison with 6° descent flight discussed in previous section and only in the inner part around the fuselage small difference in the tip vortex trajectory is visible in the figure.

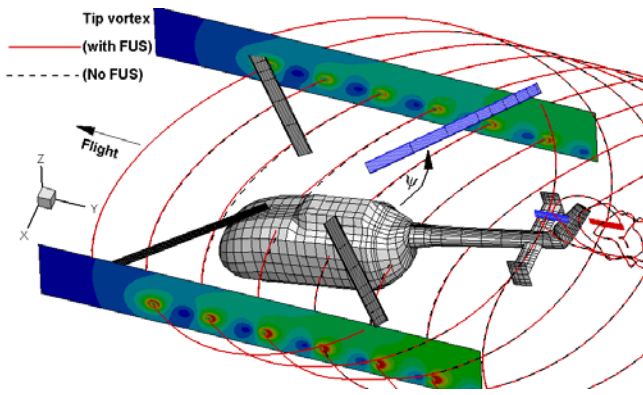


Figure 16. Perspective top view of the development of MR tip vortex with the reference blade at 40° azimuth

The enlarged closer view of the tip vortex in the advancing side shows again the effect of the fuselage has slightly slow down the convection of the tip vortex. The effect of the fuselage on MR is much small in this flight condition in comparison with previous descent flight.

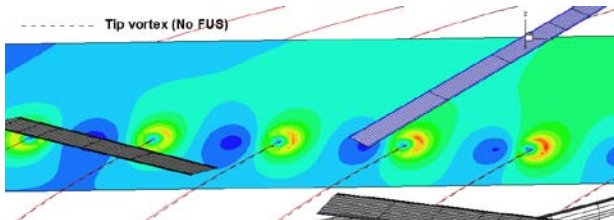


Figure 17. Enlarged closer view of the tip vortex in the advancing side BVI position at 40° azimuth

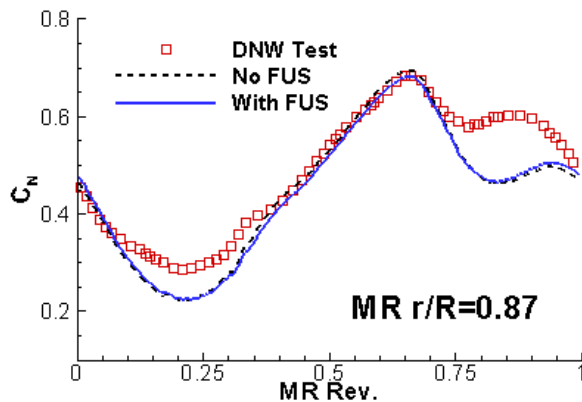


Figure 18. MR Sectional normal load

The MR sectional normal loads C_N at 87% radial station is given in Figure 18 for this flight condition. Both the experimental and simulation results as shown in Figure 18 indicate a low-frequency behavior throughout the revolution with a drop in the load occurring around 240° or MR Rev.=0.67 due to the interaction of the blade with the tip vortex trailed by the preceding blade. The two sets of predictions track each other pretty closely and inclusion of

the fuselage improves slightly the correlation against the measured data mainly around maximum peak region.

The complex flow surrounding the TR poses an extreme challenge for both experimental and theoretical study. Taken at MR reference blade located at 30° azimuthal angle, Figure 19 shows the velocity field induced by MR tip vortex on longitudinal cutting plane located on the suction side of the tail rotor 108mm away from the TR disk. MR tip vortices released from different MR blade are drawn in different color; for example MB1 indicated tip vortex released from MR blade 1. The main rotor tip vortex enters in the middle of the left side and is convected downstream and downwards to the right as indicated from measured MR vortex flight path shown in Figure 20. The prediction of the MR tip vortex flight path traces approximately the same trend as the experiment.

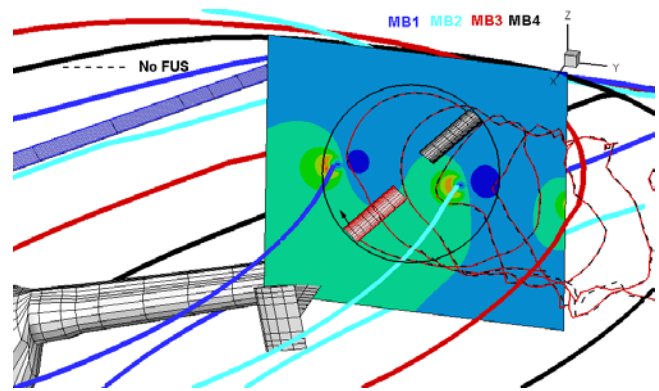


Figure 19. Flow field induced by MR tip vortex and MR/TR tip vortex trajectories at MR reference blade 30° azimuth

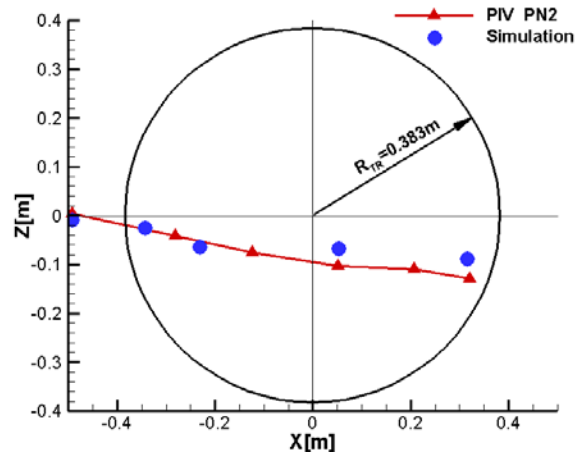


Figure 20. Comparison of measured and simulated MR vortex flight path through the tail rotor disk

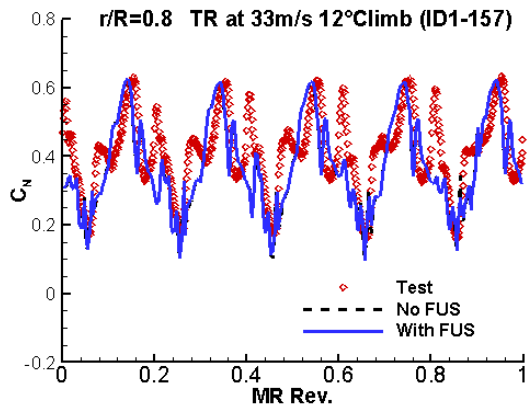


Figure 21. TR Sectional normal load at 5 TR Rev.

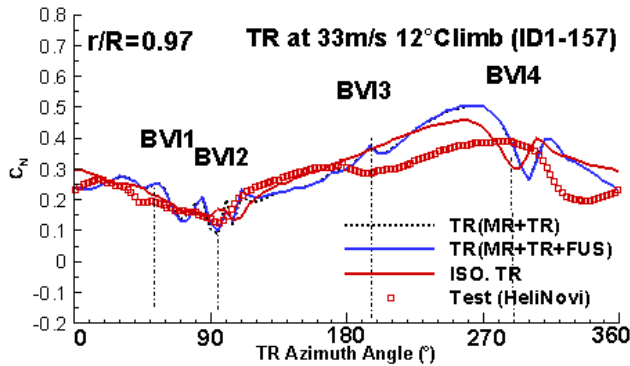
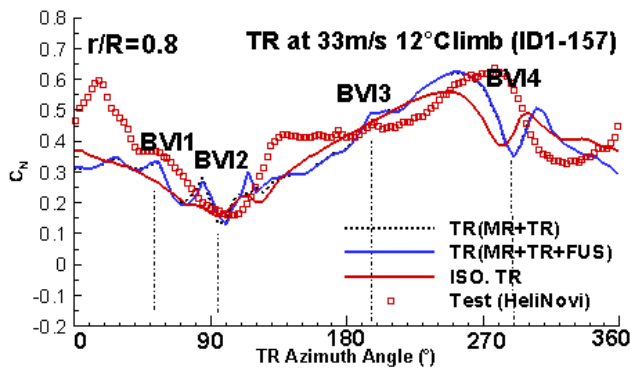


Figure 22. TR Sectional normal load at one TR rev.

The TR sectional normal loads C_N at the radial section $r/R=0.80$ is given in Figure 21. The azimuth angle of the TR is defined as zero if the TR reference blade (red shown in Figure 19) points downstream. Since the TR rotates five times faster than the MR, the representation of C_N corresponds to one complete MR revolution. Both the experimental (averaged) and simulation results show a sequence of C_N maxima and minima within each TR revolution for both flight conditions. Due to the existence of MR/TR interaction, C_N of TR varies with the TR revolutions. The numerical analysis indicates the presence of slight phase shifts in the prediction of the peak located at about 270° of TR azimuth angle, while the position of

minimum is well captured. In addition the comparison of the simulation and test indicates BVI occurred in advancing side is overestimated in the simulation.

The effect of the fuselage on TR C_N can be demonstrated more clearly in extended view in one TR revolution, as shown in Figure 22 at the radial stations $r/R=0.8$ and 0.97 . The comparison of the simulation and test indicates that BVI like peaks marked as BVI1, 2, and 4 are stronger in simulation of both with-and without fuselage. It has to be mentioned that the experiment data showing in the plot are the averaged value over more TR revolutions. Due to the possible deviation of MR and TR rotational speeds from their nominal values as well as the not completely synchronized MR-TR driving system in the experiment, the averaging can smooth the BVI peaks in the test results.

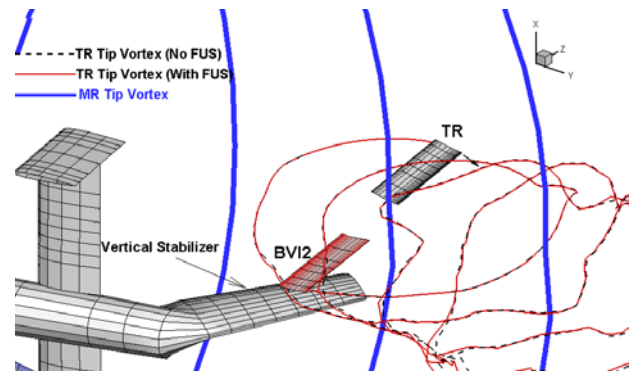


Figure 23. Closer view of TR tip vortex in TR advancing side BVI2 position

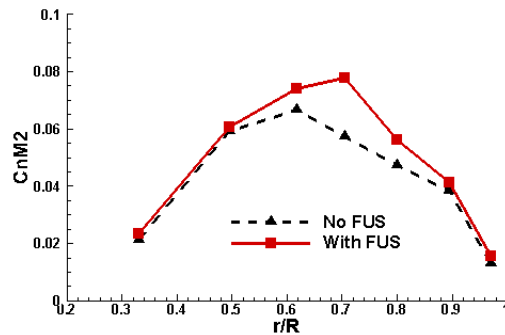


Figure 24. TR C_nM_2 spanwise distribution at TR BVI 2 position indicated in Figure 23

The effect of the fuselage which changes orientation of tip vortex relative to the TR blade is clearly visible around BVI2 where TR reference blade passes over the vertical stabilizer, as show in Figure 23 for TR azimuth angle of 100° snapshot. The changes of TR tip vortices (red solid line) is clearly shown when they pass over the vertical stabilizer. The C_nM_2 spanwise distributions at this TR azimuth position shown in Figure 24 indicate that similar to the effect of fuselage on MR, the vertical stabilizer on TR has led to high loading for all section simulated. The effect of the fuselage (the vertical stabilizer) can be neglected when TR blade away from it.

Figure 25 gives a perspective view of MR and TR tip vortices at TR azimuth position about 195° where BVI3 occurred as shown in Figure 22. The relative position among TR, MR, MR tip vortices and MR wakes (not shown in plot for clearness) indicate that the localized C_N variations around 195° is mainly caused by both the TR blade-MR tip vortex and TR blade-MR wake interactions as well as interaction between TR blade and MR potential field which become sharper for the section closer to the tip.

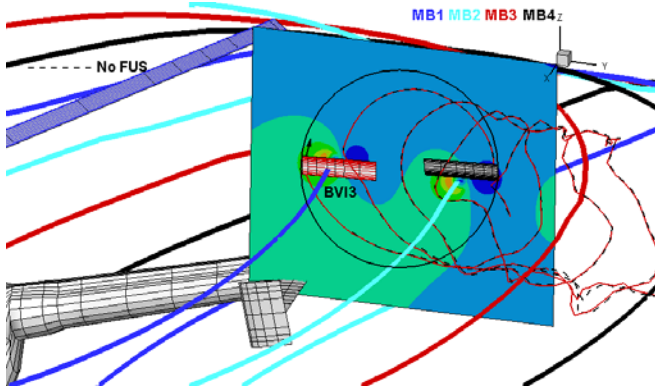


Figure 25. Perspective view of MR and TR wakes at TR azimuth position about 195° where TR perpendicular interaction with MR tip vortex occurs

In addition, the comparison of simulated TR C_N at $r/R=0.8$ and 0.97 as given in Figure 22 shows that the BVI1 and BVI2 occur at roughly same TR azimuth position for the given sections, indicating that the interaction is close to parallel one, while the azimuth position of BVI4 changes at different section imply a non-parallel interaction.

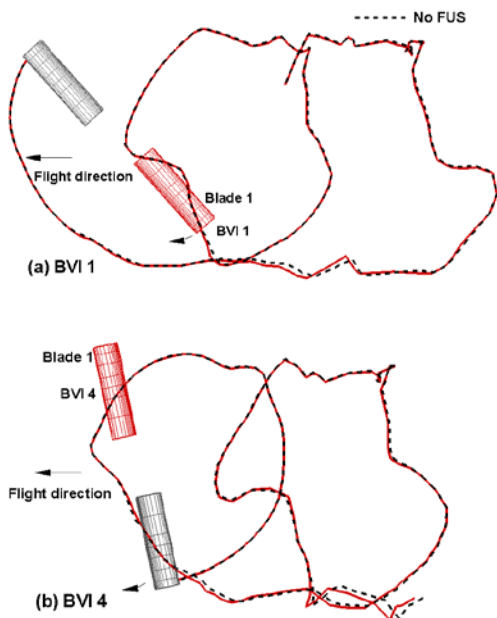


Figure 26. Snap shots of the TR tip vortex for two TR azimuth positions where BVI1 and BVI4 occur

Two snap shots of top view of the TR tip vortex under MR/TR/FUS configuration (solid line) and MR/TR configuration (dashed line) are given in Figure 26 for the azimuth positions of TR reference blade (red) where the behavior of BVI 1 and 4 are located. Both Figure 23 and Figure 26 indicate the cause of BVI 1, 2, 4 is mainly due to TR interacted with its own tip vortex (self-BVI). BVI 1 (Figure 26a) is introduced by TR blade interacted with tip vortex trailed by the proceeding blade, while BVI 2 (Figure 23) is generated due to interaction with its own tip vortex. BVI 4 causes a drop in C_N at about 270° due to the interaction of the TR blade with the tip vortex trailed by the preceding blade as shown in Figure 26b.

Figure 27 shows the tip vortex descent histories shed by TR blade 1 over first two TR revolutions. The position of the trailing edge is marked as a circle in the plot. For the comparison, also plotted in the figure are the results without fuselage, which are represented by dashed line. Until about an azimuth angle of 250° , the tip vortex of the TR (in the MR/TR/FUS configuration) follows closely the results of the TR (in MR/TR configuration). Thereafter the tip vortex of the TR (in the MR/TR/FUS configuration) deviates slightly under influence of the vertical stabilizer which causes clear difference in BVI2. The reduction of miss-distance in MR/TR/FUS configuration is responsible for the high BVI2 in this configuration. Therefore the increase of TR BVI noise is expected in rotor-fuselage configuration.

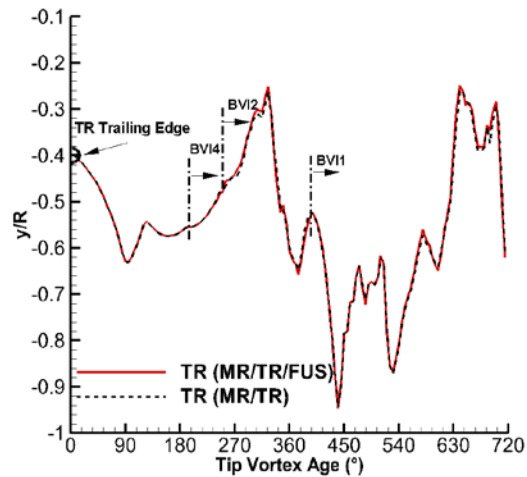


Figure 27. Tip vortex descent histories shed by TR reference blade 1 over first two TR revolutions

The full scale dBA as shown in Figure 28 was evaluated for two different configurations. The choice of full scale dBA as the metric was dictated by the necessity to highlight the TR BVI content of the spectrum. The location of the MR disc and TR rotation plane are indicated by the circle and thick line respectively. The directivity for both cases with-and without-fuselage (Figure 28 lower) look very similar and indicate two clear noisy regions located in both TR thrust-and outflow-direction. These characteristics of the noise distribution also show up in the test result (Figure 28 upper)

with a general agreement in noise level as simulation on both TR thrust- and outflow-side, but with a slightly offset in position. An additional noisy area occurs just at upstream of the TR and around TR rotational plane in the test results doesn't show up in the simulations. In general, the influence of fuselage in the simulation has caused slightly higher level in both TR thrust- and outflow-direction, which corresponds to the increase of BVI2 as observed in Figure 22.

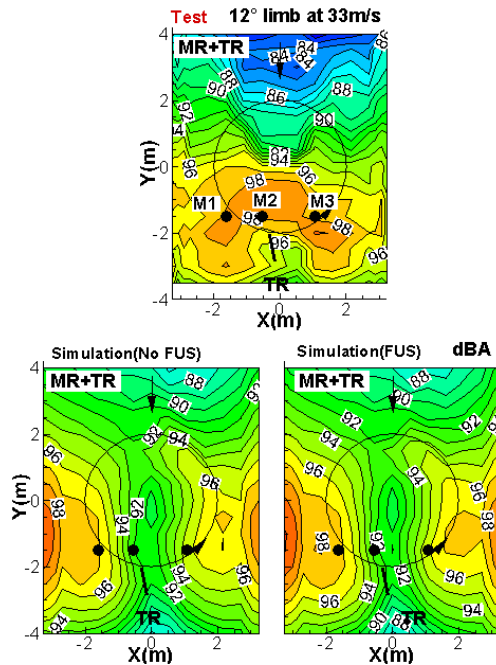


Figure 28. Simulated and measured full scale dBA contours at two different configurations

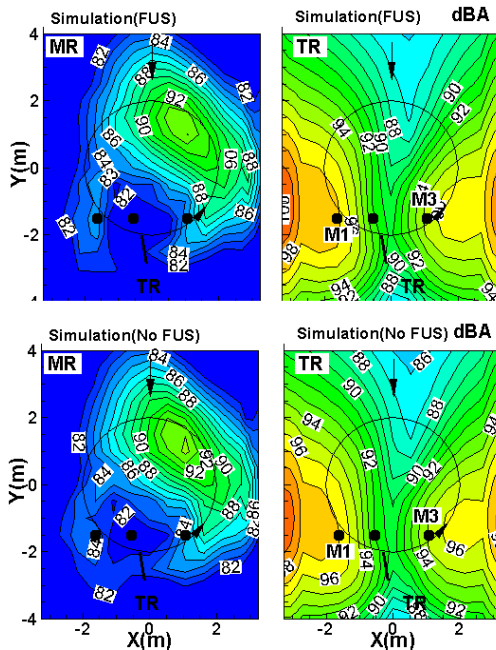


Figure 29. Simulated MR and TR contributions to total noise at two different configurations

In order to evaluate the noise contribution from each rotor, the results from both MR and TR for the simulation with and without fuselage are shown in the Figure 29. In general the TR is major source of noise for noisy regions located in TR thrust- and outflow-direction which is major contribution of TR loading noise. MR contribution is for a position ahead of the main rotor on the advancing side.

Figure 30 gives the comparisons of the acoustic pressure time histories taken from 3 microphone positions, as shown in Figure 28, where tail rotor effects are expected to be more pronounced. The time histories show a general agreement in phase of the acoustic pressure with tail rotor (10/MRrev) behavior present in both experiment and prediction. There is under prediction of sound pressure level for M1 and M2. Especially at M2, the measured acoustic pressure indicates a strong “thickness noise” type signal with a large negative peaks.

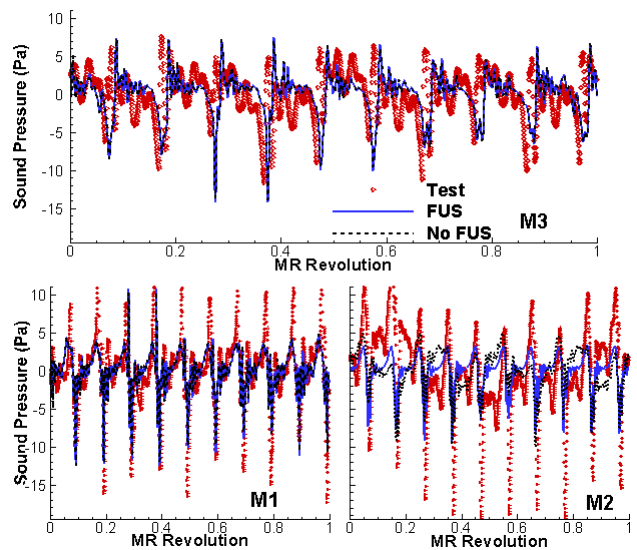


Figure 30. Acoustic pressure time histories taken from 3 microphone positions, as shown in Figure 12

3.3 60m/s level flight (ID2)

The MR sectional normal loads C_N at 87% radial station is given in Figure 31. C_N “bucket” can be observed in the experiment that extends from approximately 100° to 150° with the minimum located around 130° . This phenomenon is likely to be determined by the co-existence of important compressibility, aeroelastic and interactional effects, which was not captured in the simulation. The localized C_N variations among 45° and 90° seem to be reproduced by the physical blade-vortex interaction. The sudden drop at 270° is correctly predicted despite differences in value and location of the C_N maximum can be observed. The two sets of predictions track each other pretty closely and inclusion of

the fuselage in general improves the correlation against the measured data.

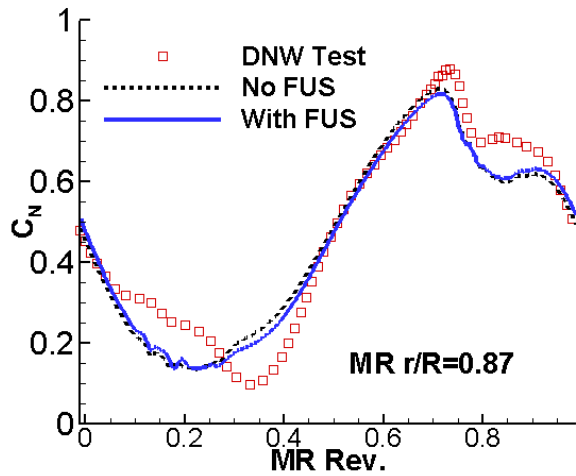


Figure 31. MR Sectional normal load in MR Rev.

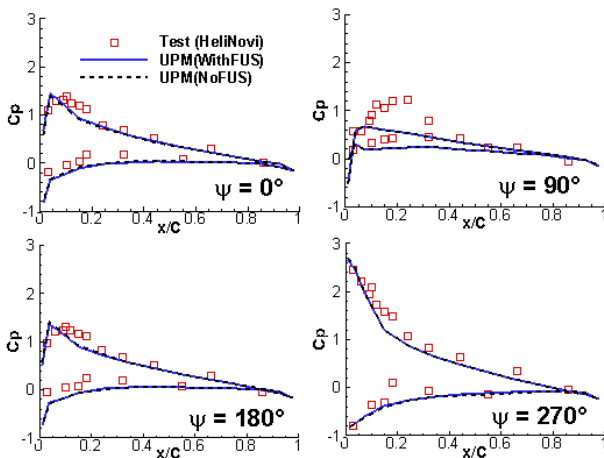


Figure 32 Computed and measured pressure distribution on main rotor at 87% blade radius at various main rotor azimuth angle

The pressure chordwise distributions at selected azimuth positions are given in Figure 32 and compared with test results. The overall agreement among the computed and measured data is satisfying, except for the azimuth angle about 90° where the strong compressible effect was not captured by UPM due to the incompressible prediction.

The TR sectional normal loads C_N at the radial section $r/R=0.80$ and 0.97 is given in Figure 33 in one complete MR revolution or 5 TR Rev. Both the experimental (averaged) and simulation results show a sequence of C_N maxima and minima within each TR revolution. Due to the existence of MR/TR interaction, C_N of TR varies with the TR revolutions. A good correlation of C_N with the experiment is shown.

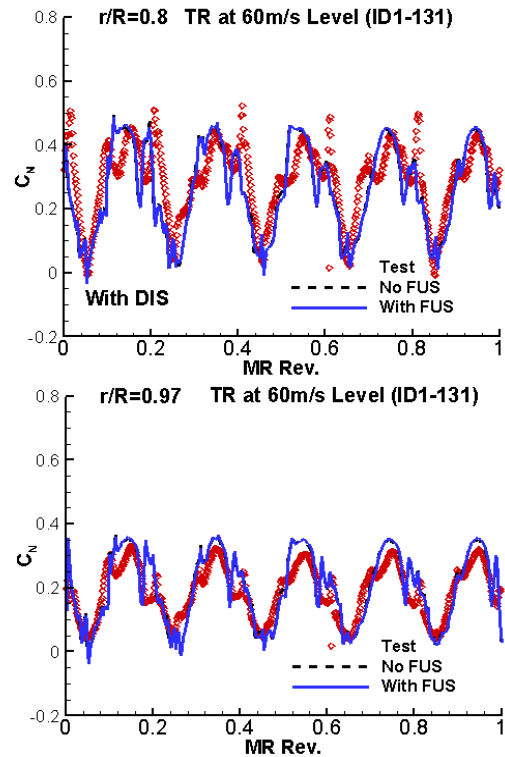


Figure 33. TR Sectional normal load at 5 TR Rev.

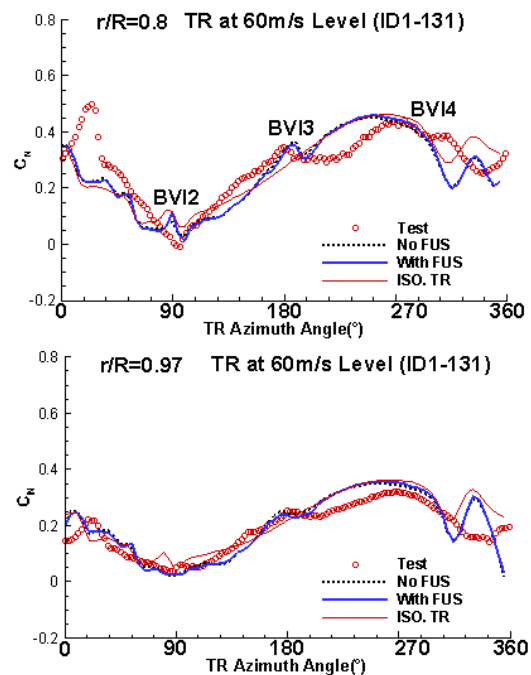


Figure 34. TR Sectional normal load at one TR rev.

The effect of the fuselage on TR C_N can be demonstrated more clearly in extended view in one TR revolution, as shown in Figure 34 at the radial stations $r/R=0.8, 0.97$. As similar to the climb condition, the comparison of the simulation and test indicates that BVI like peaks located in

1st quadrant are stronger in simulation for both with-and without fuselage. The effect of the fuselage has slightly increasing BVI2 peaks in 1st quadrant when the TR reference blade (red) passes over the vertical stabilizer, as show in Figure 35 for TR azimuth angle of 100°. The changes of TR tip vortices (red solid line) is clearly shown when they pass over the vertical stabilizer. In comparison with the climb condition in Figure 23, BVI2 in this flight condition becomes more localized or non-parallel one, while the characteristics of BVI3 and BVI4 remain the same in both flight conditions. The CnM2 spanwise distributions at this TR azimuth position shown in Figure 36 indicate a complicated distribution with decreasing blade loading near blade tip region.

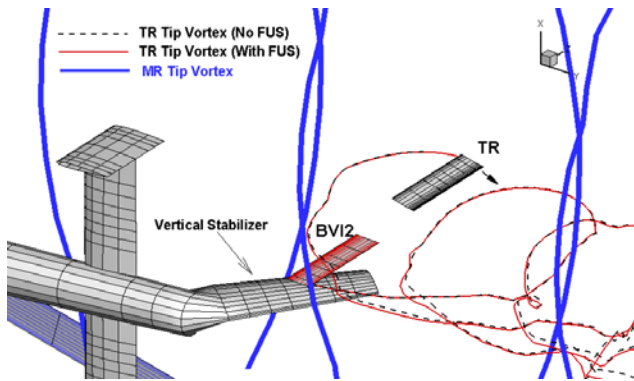


Figure 35. Closer view of TR tip vortex in TR advancing side BVI2 position

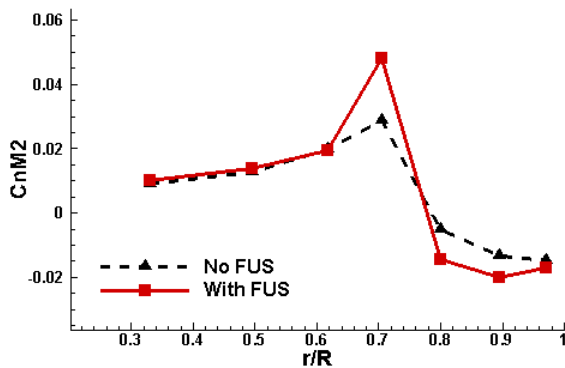


Figure 36. TR CnM2 spanwise distribution at TR position indicated in Figure 35

Figure 37 shows the comparison of the simulated and measured full scale dBA contours for 60m/s level flight. The directivity for both cases with-and without-fuselage (Figure 37 lower) look very similar and indicate the two clear noisy regions located in both TR thrust- and outflow-direction. The influence of fuselage in the simulation has in general caused slightly higher level in a large area in both TR thrust- and outflow-direction. The comparison with the test results shows that there is a good comparison in terms of the maximum noise level and general characteristics of the noise directivity.

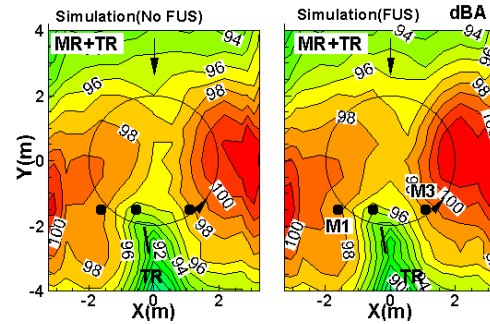
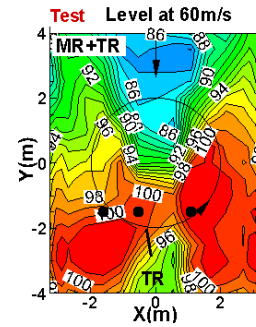


Figure 37. Simulated and measured full scale dBA contours for 60m/s level flight

For both configurations with-or-without the fuselage, the simulated contribution of TR and MR noise (Figure 38) indicate that the TR is major source of noise in 60m/s level flight in the region of TR thrust- and outflow-direction, while MR noise (Figure 38 left) also play an important role in MR advancing blade side.

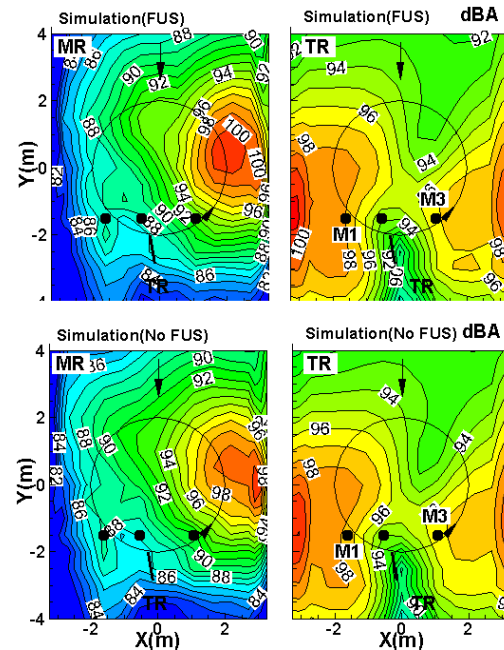


Figure 38. Simulated full scale dBA contours for MR and TR at two different configurations

The higher noise level under the influence of fuselage in the simulation corresponds to the increase of TR BVI2 as observed in Figure 34 as well as increasing MR noise. In comparison with the 12° climb case, the higher MR and TR noise level are observed which can be considered as increasing local tip Mach number.

3.4 Change TR rotational direction at 12° climb with 33m/s flight speed

The original BO105 TR configuration is rotated in Advancing Side Down (ASD) direction as shown in Figure 39 left, however both Bo105 HeliNovi campaign [15,16] and the simulations [7] found that, in climbing flight and in level forward flight, the mean noise level of the helicopter with Advancing Side Up (ASU) (Figure 39 right) configuration was lower. As previous numerical studies [7] were based on MR/TR configuration, the numerical results from MR/TR/FUS configuration will be presented in this section. The TR with a NACA0012 profile is used.

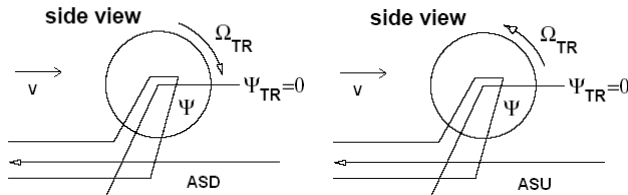


Figure 39. Different TR rotational direction (Circle represents TR disk), left: Advancing Side Down (ASD); right: Advancing Side Up (ASU)

The TR sectional normal loads C_N at the radial section $r/R=0.97$ are given in Figure 40 for one complete MR revolution or 5 TR revolutions for both ASD and ASU conditions. Both the experimental and simulation results show a good correlation in C_N maxima and minima within each TR revolution for TR in ASD mode, as shown in Figure 40 upper, while for TR in ASU mode there is underestimation on minimum C_N value in advancing blade side for all revolution, as shown in Figure 40 lower.

Figure 41 shows the comparison of C_N for one TR rotation in both ASD and ASU. As for the case where TR equipped with S102E blade (Figure 22 lower), Figure 41 lower shows TR equipped with NACA0012 blade has similar BVIs occurrence in both advancing and retreating TR blade side. When comparing with the test results, similar BVIs in advancing side are also observed in the test, but relative weaker in amplitude. The comparison of the simulation and test shows the maximum loads matched well, but a phase shift on the level drop down in retreating side indicates a delayed BVI occurrence in the test, as explained in previous section for Figure 22. As indicated from previous section, the effect of the fuselage on TR blade loads is strongest when TR blade passes over the vertical stabilizer. Therefore, clear TR/vertical stabilizer interaction is observed for TR ASU mode in blade retreating side around 270° azimuth angles too as shown in Figure 41 lower.

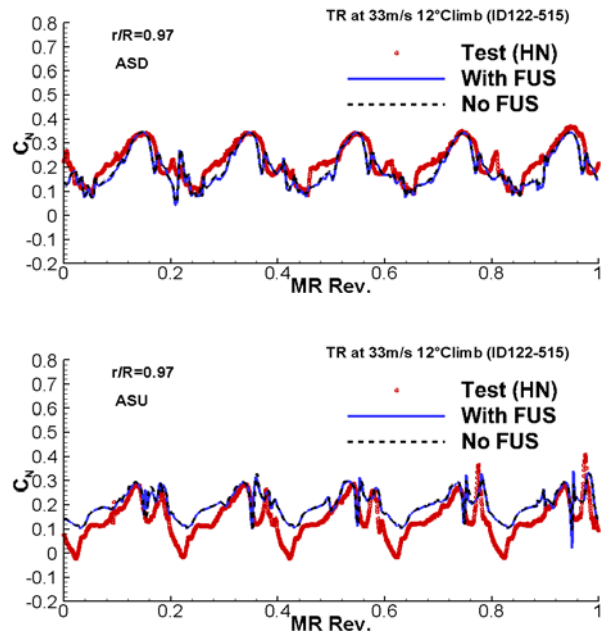


Figure 40. TR Sectional normal load at one MR or 5 TR revolution for TR rotation in ASD and ASU

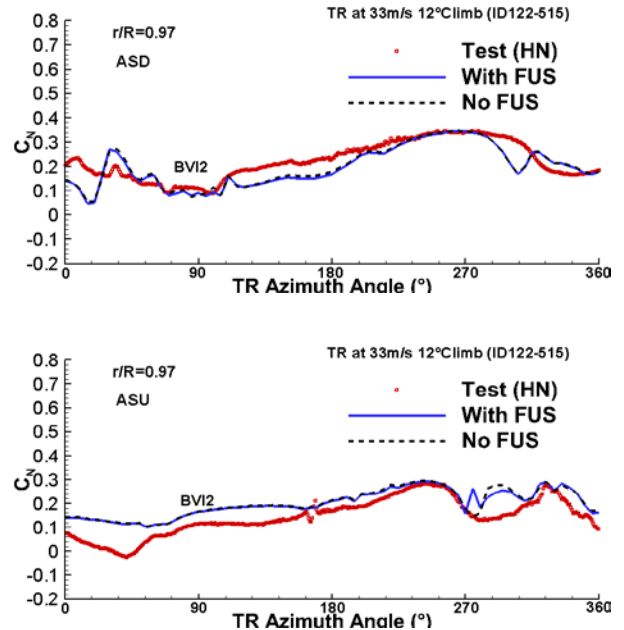


Figure 41. TR Sectional normal load at one TR revolution for TR rotation in ASD and ASU

When comparing with C_N for TR in ASD mode, the numerical analysis of C_N time history in ASU condition as shown in Figure 41 (lower) shows a dramatic reduction of BVI amplitude and number of BVIs in the advancing blade side.

The snap shot of the TR tip vortex for TR in ASD and ASU mode are given in Figure 42 at TR azimuth positions where the BVI2 occurs in TR ASD mode, as shown in Figure 41. Instead of almost parallel BVI occurring in TR ASD mode

as shown in Figure 42 upper, the interaction occurring for this azimuth angle is almost perpendicular in TR ASD mode as shown in Figure 42 lower, which explains disappearing of BVI2 in advancing side in TR ASU mode.

Although there is increasing in number of BVIs in the retreating side of ASU mode, the tip Mach number for the retreating blade side is smaller than that for the advancing blade side. Therefore the reduction of the blade loading noise is expected in ASU blade mode, as from the Ffowcs-Williams Hawking’s acoustic analogy theory, loading noise is strongly dependent on unsteady blade loads, especially in advancing blade side. The reduction in these C_N peaks is beneficial for the noise reduction.

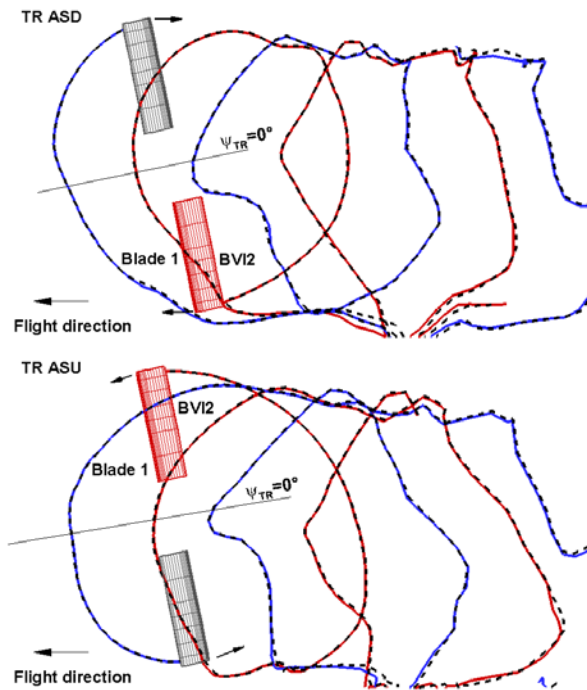


Figure 42. Snap shots of TR tip vortex for TR in ASD and ASU mode at TR azimuth positions where the BVI2 occurs in TR ASD mode

Figure 43 shows the tip vortex descent histories shed by TR blade 1 for ASD and TR blade 2 for ASU. The choice of the tip vortex from the different blade is according to the interaction characteristics given in Figure 42. The azimuth positions and the interaction duration are marked as vertical dashed lines. In addition to the favorite BVI orientation in TR ASD mode, the miss distance of BVI2 in TR ASD mode is also smaller than that in TR ASU mode. The tip vortex of the TR (in the MR/TR/FUS configuration) follows closely the results of the TR (in MR/TR configuration) for both TR ASD and ASU mode and only slightly deviation was found when tip vortices approach the vertical stabilizer.

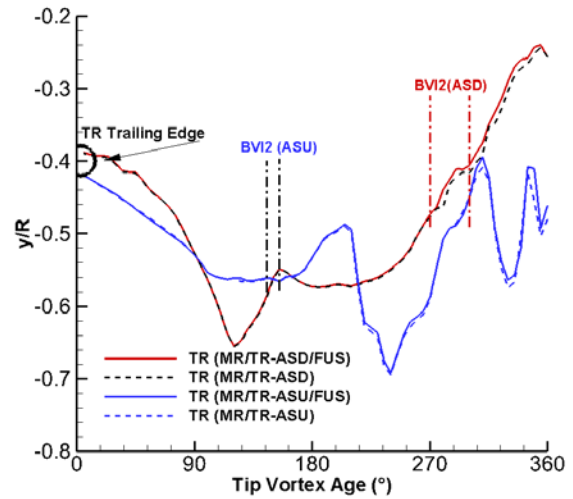


Figure 43. Tip vortex descent histories shed by TR blade 1 for ASD and TR blade 2 for ASU over first TR revolution

The influence of the different TR rotation direction on TR noise radiation can be demonstrated by observing noise contour plots as shown in Figure 44 and Figure 45 for TR rotating in ASD and ASU respectively. As indicated from previous section that TR is major source of noise, therefore only contribution from TR is given. In general, two different TR rotating directions result in significant difference in the noise directivity.

The comparison of the test results for TR rotating in ASD mode (Figure 44 upper) and in ASU mode (Figure 45 upper) shows that in general the differences occur in two different regions. The first region is located in TR thrust- (marked as Max 3) and outflow-direction (marked as Max 1) where the contribution from TR loading noise is expected. In TR rotating in ASU mode, significant noise reduction in this region is observed which is due to the reduction of BVI amplitude and number of BVIs occurring in the advancing blade side as shown in Figure 41. In addition to the reduction of the noise level at location Max 1 and Max 3, there is also slight shift of noise regions (Max 1 and Max 3) to further downstream in TR ASU mode because of high noise source position in advancing side and less Doppler amplification towards this direction for TR rotating in ASU mode. The second region is located at upstream of the TR around TR rotational plane (marked as Max 2). In this region, both the noise reduction and shift of noise region to the upstream is observed in TR rotating in ASU mode.

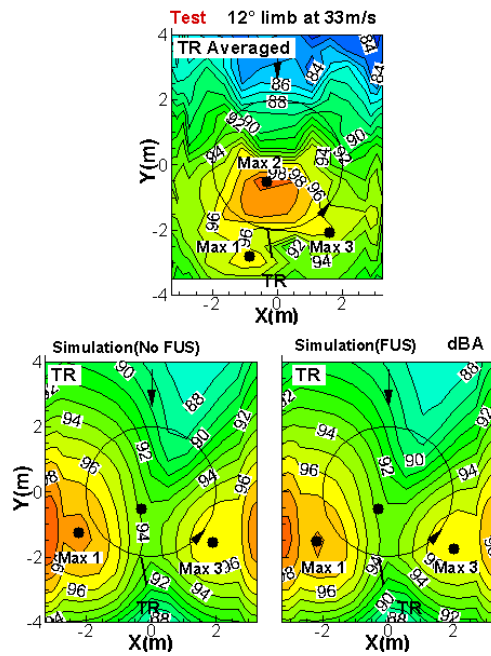


Figure 44. Simulated and measured full scale dBA contours for TR rotating in ASD

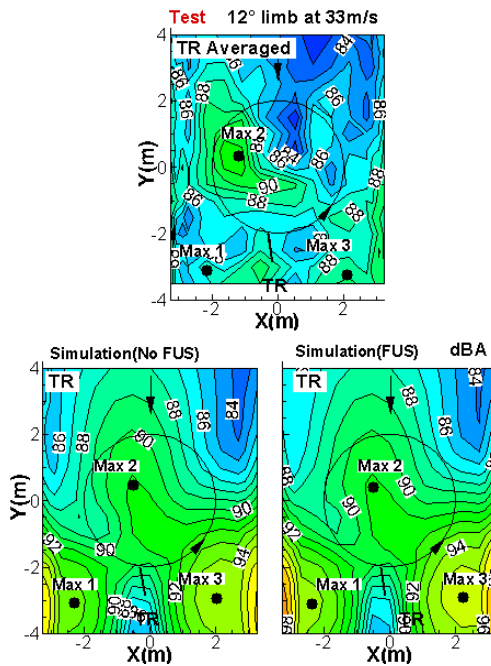


Figure 45 Simulated and measured full scale dBA contours for TR rotating in ASU

The comparisons of the simulation results for TR rotating in ASD mode (Figure 44 lower) and in ASU mode (Figure 45 lower) show in general the two regions mentioned in the test, where the noise reduction occurred, are captured for both configuration with-and -without fuselage, although there is over-estimation in TR loading noise located at Max1 and Max 3 in the simulation. In TR ASU mode, the comparison of simulated TR noise (Figure 45 lower) with the test

(Figure 45 upper) shows both directivities bear good similarity in the hot spot region Max 2. The simulated contour plot from TR rotating in ASU mode indicate a similar high noise region (Marked as Max 2) at upstream of the TR as in the test. The comparison of time history at this position as shown in Figure 46 indicates TR thickness noise is main contributor to the noise in this region.

In general, the influence of fuselage has caused slightly increasing maximum TR loading noise about 0.5dBA for TR ASU mode due to higher retreating side BVI while influence on maximum noise level for TR ASD can be neglected.

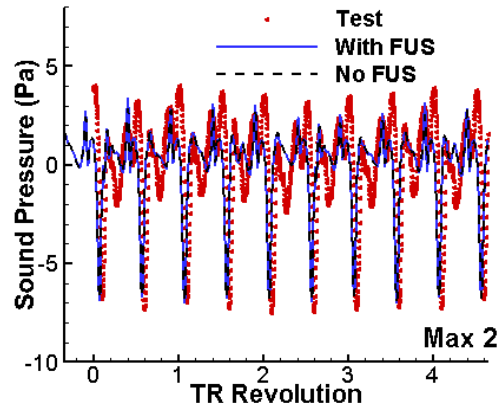


Figure 46. Acoustic pressure time histories taken from Max2, as shown in Figure 45

As TR noise contribution can be further separated into the contribution from the thickness noise and the loading noise respectively, the TR's acoustic contribution represented as thickness noise, loading noise under MR/TR/FUS configuration for two different sense of TR rotation are demonstrated in Figure 47 and Figure 48.

For both TR ASD and ASU rotational direction, TR loading noise is the dominate source of noise along both sides of the tail rotor rotational plane (Max1 and Max 3) while the TR thickness noise shows a symmetric pattern with the maximum area directly in the tail rotor rotational plane (Max 2). When comparing with the results of TR rotating in ASD mode (Figure 47 right), TR loading noise level for TR rotating in ASU mode (Figure 48 right) is reduced and maximum area is also shifted further downstream, while the maximum area of the TR thickness noise (Figure 48 left) is slightly shifted upstream and magnitude of new maximum area is reduced. As the reduction of TR loading noise in ASU mode, the contribution of TR thickness noise to overall TR noise given in Figure 45 (lower) becomes evident. This characteristic is also observed in the measurement results.

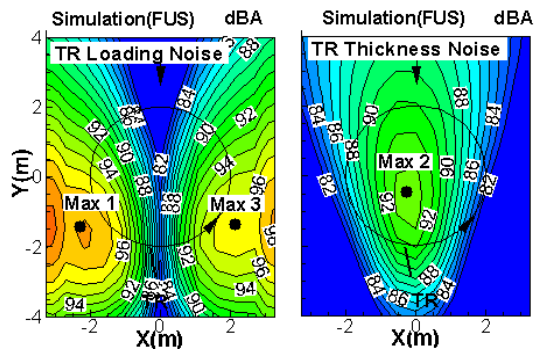


Figure 47. Simulated TR thickness (right) and loading (left) noise under MR/TR/FUS configuration in TR ASD

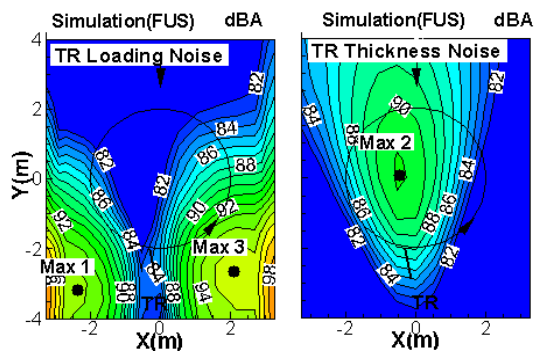


Figure 48. Simulated TR thickness (right) and loading (left) noise under MR/TR/FUS configuration in TR ASU

The reasons for the reduction of TR noise for TR rotating in ASU mode are mainly twofold. First, lack of strong BVI in advancing blade side in ASU mode is observed when comparing with that occurs in ASD mode, as shown in Figure 41. Although there are obviously BVI peaks occurring on the retreating side in ASU mode, from an acoustics point of view the interactions on the advancing side as occurred in ASD mode are dominant due to the locally higher Mach numbers. Second, the Mach number of the source in the observer direction is different for the same observer in ASD and ASU mode. It is obviously that the less noise is observed at the observers upstream in ASU mode, because the Doppler amplification factor is less than unity for a receding subsonic source. Therefore TR radiates less noise in upstream direction. In addition, increasing the advancing blade distance in ASU mode will reduce TR thickness noise and shift the peak upstream.

CONCLUDING REMARKS

A DLR methodology using an unsteady free wake panel method (UPM) and a Ffowcs Williams-Hawkings (FW-H)-equation based code, APSIM was applied in aeroacoustic simulations of a helicopter with MR/TR/Fuselage. The tip vortex core radius development model derived from experiment has been calibrated and an initial vortex core radius of $0.3c$ is chosen in the simulation.

The influence of fuselage on MR and TR noise at three different flight conditions were presented and compared with test results. The noise reduction techniques including TR sense of rotation (NACA 0012 TR used) was analyzed. The following conclusions are drawn from the results and discussion presented:

1. 6° descent flight where MR is major source of noise

Inclusion of the fuselage improves clearly the correlation against the measured data in 2nd and 3rd quadrant of MR revolutions. The influence of fuselage has in general caused a reduction of maximum MR BVI in both advancing and retreating side as the effect of the upwash of the fuselage is to slow down the rotor downwash and the convection of the tip vortex towards the blade is reduced in rotor-fuselage case, which increases slightly miss distance of the tip vortex to the blade. The azimuth positions of BVI were hardly changed under the influence of the fuselage.

2. Low speed climb and high speed level flight where TR is major source of noise

For MR, inclusion of the fuselage improves slightly the correlation against the measured data mainly around maximum peak region. For TR, the effect of the fuselage increases slightly TR BVI at advancing side when TR blade passes over the vertical stabilizer and therefore causes increasing TR BVI noise.

3. Change TR rotational direction at low speed climb

The study on change TR rotational direction indicated aerodynamic interaction between the main and tail rotors is sensitive to the tail rotor rotational direction. The reduction of TR BVI amplitude and number of TR BVIs on the advancing TR blade side in TR rotating in Advancing Side Up (ASU) is the cause of a significant aerodynamically-induced loading noise reduction.

In general, the influence of fuselage has caused slightly increasing maximum TR loading noise about 0.5dBA for TR ASU mode while influence on maximum noise level for TR ASD can be neglected.

The comparison between the experimental results and the numerical ones highlighted once more the extreme complexity of the aerodynamic phenomena involved in a complete helicopter configuration operating at different flight conditions.

REFERENCES

- [1] Jacobs, Eric W.; Fitzgerald, James M.; Shenoy, Rajarama K. "Acoustic characteristics of tail rotors and the effects of empennage interactions", AHS, Annual Forum, 43rd, Saint Louis, MO, May 18-20, 1987, Proceedings. Volume 1 (A88-22726 07-01). Alexandria, VA, American Helicopter Society, 1987, p. 437-451.

- [2] Joon W. Lim and Arsenio C. B. Dimanlig, "The Effect of Fuselage and Rotor Hub on Blade-Vortex Interaction Airloads and Rotor Wakes", Presented at the 36th European Rotorcraft Forum, Paris, France, September 7-9, 2010. Paper Number 051
- [3] Boyd, D. D., "HART-II Acoustic Predictions using a Coupled CFD/CSD Method", American Helicopter Society 65th Annual Forum Proceedings, Grapevine, Texas, May 27-29, 2009
- [4] Jung Hwan Sa, Young-Hyun You, Jae-Sang Park, Sung Nam Jung, Soo Hyung Park and Yung H. Yu, "Assessment of CFD/CSD Coupled Aeroelastic Analysis Solution for HART II Rotor Incorporating Fuselage Effects". American Helicopter Society 67th Annual Forum, Virginia Beach, Virginia, May 3-5, 2011.
- [5] Yin, J., Ahmed S.R., "Helicopter main-rotor/tail-rotor interaction", Journal of the American helicopter society, Vol.45, No.4, pp293-302, October 2000.
- [6] Fletcher, T. M., Duraisamy, K. and Brown, R. E., "Sensitivity of Tail Rotor Noise to Helicopter Configuration in Forward Flight", 65th AHS Annual Forum, Grapevine, Texas, USA, May 27-29, 2009.
- [7] Yin, J., "Simulation of Tail Rotor Noise Reduction and Comparison with HeliNovi Wind Tunnel Test Data", 67th AHS Annual Forum, May 3-5, 2011
- [8] Stefano Melone and Andrea D'Andrea, "Helicopter Main Rotor - Tail Rotor Interactional Aerodynamics and Related Effects on the On-Ground Noise Footprint". Presented at the 37th European Rotorcraft Forum, Vergia, Italy, September 13-15, 2011.
- [9] George, A.R. and Chou, S.T., "A Comparative Study of Tail Rotor Noise Mechanisms", 41st AHS Annual Forum, Fort Worth, Texas, May 1985.
- [10] Amiet, R.K., "Airfoil Gust Response and the Sound Produced by Airfoil-Vortex Interaction", AIAA Paper 84-2268, Oct. 1984.
- [11] Tadghighi, H., "An Analytical Model for Prediction of Main Rotor/ Tail Rotor Interaction Noise", AIAA Paper 89-1130, April 1989.
- [12] Quackenbush, T. R., Bliss, D.B. and Mahajan, A., "High Resolution Flow Field Prediction for Tail Rotor Aeroacoustics", 45th AHS Annual Forum, Boston, MA, May 1989.
- [13] Baron, M. and Boffadossi, M., "Unsteady Free Wake Analysis of Closely Interfering Helicopter Rotors", Paper No. 108, 19th European Rotorcraft Forum, Cernobbio, Italy, Sept. 14-16, 1993.
- [14] Bagai, A. and Leishman, G.J., "Free-Wake Analysis of Tandem, Tilt-Rotor and Coaxial Rotor Configurations", 51st AHS Annual Forum, Fort Worth, Texas, May 9-11, 1995.
- [15] Yin, J. und Buchholz, H. und Spletstößer, W. "Numerical Simulation of Bo105 Main/Tail Rotor Interaction Noise and Preliminary Comparisons with Flight Test Results", 28th European Rotorcraft Forum, Bristol (gb), 17.-20.09.2002
- [16] Langer, H.-J., Dieterich, O., Oerlemans, O., Schneider, O., v.d. Wall, B., Yin, J., "The EU HeliNOVI Project -Wind Tunnel Investigations for Noise and Vibration Reduction", 31st European Rotorcraft Forum, Florence, Italy, 2005.
- [17] Yin, J., van der Wall, B., and Oerlemans, S., "Representative Test results from HELINOVI Aeroacoustic Main Rotor/Tail Rotor/Fuselage Test in DNW"; 31st European Rotorcraft Forum; FIRENZE, Italy; Sept. 13-15, 2005.
- [18] J.E. Ffowcs Williams, D.L. Hawkings, "Sound Generation by Turbulence and Surfaces in Arbitrary Motion", Philosophical Transactions of the Royal Society, A264, 1969
- [19] Yin, J. and Delfs, J., "Improvement of DLR Rotor Aero-acoustic Code (APSIM) and its Validation with Analytic Solution", 29th European Rotorcraft Forum, Friedrichshafen, Germany, 2003
- [20] Yin, J., Kuntz, M. and Delfs, J., "Prediction of Acoustic Far Field with DLR's Acoustic Code APSIM", APSIM manual for version 7.0 – December 2, 2008.
- [21] Brooks, T., F., "Aeroacoustic codes for rotor harmonic and BVI noise - CAMRAD.Mod1/HIRES", AIAA 96-1735, 2nd AIAA/CEAS Aeroacoustics Conference, May 6-8, 1996.
- [22] Rahier, G. and Delrieux, Y.: Blade-vortex interaction noise prediction using a rotor wake roll-up model, Journal of aircraft, Vol.34, No.4, July, 1997.
- [23] van der Wall, B.G. and Yin, J. "DLR's S4 code validation with HART II data", HART II workshop, Sept. 11, 2006.